Optimization of the $N_{\parallel}$ Upshift in the DIII-D high field side lower hybrid current drive experiment

OPEN ACCESS
IOP Publishing
Plasma Physics and Controlled Fusion
Plasma Phys. Control. Fusion **66** (2024) 065024 (6pp)
https://doi.org/10.1088/1361-6587/ad44d6

Optimization of the $N_{||}$ Upshift in the DIII-D high field side lower hybrid current drive experiment

Grant Rutherford*, Samuel J Frank[1], Andrew H Seltzman, Paul T Bonoli and Stephen J Wukitch

Plasma Science and Fusion Center, Massachusetts Institute of Technology, 190 Albany Street, Cambridge, MA 02139, United States of America

E-mail: grantr@mit.edu

Received 21 February 2024, revised 10 April 2024
Accepted for publication 29 April 2024
Published 9 May 2024

Abstract

High field side lower hybrid current drive (LHCD) is one potential candidate for efficient non-inductive current drive in tokamak power plants, and the first test of this technology will occur on the DIII-D tokamak during the 2024 campaign. Previous LFS launch experiments operated in the multi-pass regime and relied on scrape-off layer interactions to close the spectral gap. In the DIII-D experiment, single-pass damping is achievable via an upshift in the parallel refractive index $N_{||}$ caused by mode converting twice (slow $\rightarrow$ fast $\rightarrow$ slow). This mode conversion affects the ray trajectories and can lead to enhanced $N_{||}$ upshift depending on where mode conversion occurs. Compared to multi-pass absorption experiments, the optimization of launched $N_{||}$ and plasma parameters can be counter-intuitive: increased density may increase efficiency and smaller $N_{||,\mathrm{launch}}$ tend to damp closer to the separatrix. A hard x-ray camera installed to measure the bremsstrahlung (50–250 keV) radiation from LHCD-generated fast electrons is capable of verifying the trends reporting in this paper through comparison to the ray-tracing/Fokker–Planck codes GENRAY/CQL3D.

Supplementary material for this article is available online

Keywords: high field side launch, lower hybrid current drive, DIII-D tokamak, mode conversion

1. Introduction

Tokamak power plants will require some form of efficient, non-inductive current drive for current profile tailoring, instability mitigation, and/or pulse extension. Using slow waves to Landau damp on fast electrons, lower hybrid current drive (LHCD) [1] is highly efficient at driving noninductive current and is an attractive option for reactors [2]. If operated at high density and in the multi-pass regime, the efficiency can be reduced due to significant power loss in the scrape-off layer (SOL) [3–5]. While this effect should be less pronounced in reactors due to strong single-pass damping from the high temperatures, it does impact the ability to study LHCD in present tokamaks. No LHCD experiment has yet operated outside of the multi-pass regime due to insufficient temperature and/or upshift of the parallel refractive index ($N_{||}$).

However, the new DIII-D high field side (HFS) LHCD experiment [6] is predicted to achieve single-pass damping for the first time and across a wide range of plasma parameters [7]. The launcher was optimized for $N_{||,\mathrm{launch}} = -2.7$ at 4.6 GHz and is capable of coupling up to 1 MW in this forward lobe [8]. Here, $N_{||} = k_{||}c/\omega$ is the refractive index of the LH wave parallel to the background magnetic field, where c is the speed of light, $k_{||}$ is the parallel wave vector, and ω is the wave's angular

[1] Current affiliation is Realta Fusion.
* Author to whom any correspondence should be addressed.

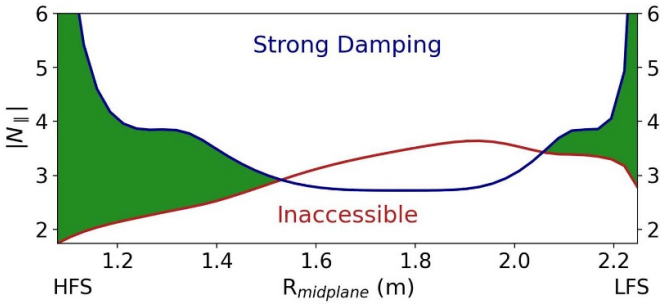

Figure 1. Shaded in green is where LH waves may propagate as slow waves at the midplane of DIII-D discharge 147634. Increasing $|N_\parallel|$ above this region leads to rapid damping, and decreasing $|N_\parallel|$ causes mode conversion.

frequency. By varying the phase between the klystrons powering the launcher modules, $N_{\parallel,\mathrm{launch}}$ can be varied from -2.3 to -3.1 before the directivity drops below $\sim$50%. The purpose of the HFS LHCD system is to drive current between $\rho = 0.6 - 0.8$ to produce the broad current profiles relevant to advanced tokamak plasmas. To successfully drive current within this region, the processes that modify the LH waves' $N_\parallel$ must be well understood. For the DIII-D experiment, $N_\parallel$ is expected to evolve mainly due to geometrical and mode conversion effects.

As a LH wave propagates in a torus, $N_\parallel$ changes due to the poloidal asymmetry of the toroidal magnetic field, B_T, which prevents the wave's poloidal mode number, m, from being conserved. Thus, $N_\parallel$ varies along the ray trajectory according to

$$N_\parallel \approx \frac{c}{\omega}\frac{m}{R_0 q} + \frac{c}{\omega}\frac{n}{R} = N_\theta + N_\phi, \tag{1}$$

where a circular cross section and $B_{\mathrm{total}} \approx B_{\mathrm{T}}$ are assumed and R is the major radius, R_0 is the major radius of the magnetic axis, q is the safety factor, and n is the toroidal mode number [9]. For the LH wave to remain a propagating slow wave, $|N_\parallel|$ must remain larger than the accessibility condition where the fast and slow waves converge, N_{acc} [10], and smaller than the value at which significant quasilinear electron Landau damping occurs, N_{ELD} [11]:

$$|N_\parallel| > N_{\mathrm{acc}} \approx \frac{\omega_{\mathrm{pe}}}{\Omega_{\mathrm{e}}} + \sqrt{1 - \frac{\omega_{\mathrm{pi}}^2}{\omega^2} + \frac{\omega_{\mathrm{pe}}^2}{\Omega_{\mathrm{e}}^2}} \propto \frac{\sqrt{n_{\mathrm{e}}}}{B} \tag{2a}$$

$$|N_\parallel| < N_{\mathrm{ELD}} \approx \frac{5.8}{\sqrt{T_{\mathrm{e}}}} \propto \frac{1}{\sqrt{T_{\mathrm{e}}}}, \tag{2b}$$

where ω_{pe} is the electron plasma frequency, Ω_{e} is the electron cyclotron frequency, ω_{pi} is the ion plasma frequency, n_{e} is the electron density, B is the total magnetic field, and the scalings are given to first order. These inequalities form an operational window in which the LH waves may exist. An example of this window at the midplane of DIII-D discharge 147634 is given in figure 1. The 1/B dependence of N_{acc} was a driving motivation for moving the LH launcher to the HFS on DIII-D as the higher local B decreases N_{acc} and allows smaller $|N_\parallel|$ to penetrate into the plasma [12]. This has the benefit of more efficient current drive as the current drive efficiency $\eta_{\mathrm{CD}} = e/(m v_\parallel \nu(v)) \propto 1/N_\parallel^2$, where e is the elementary charge, $v_\parallel$ is the parallel velocity of the accelerated electron, and ν is the momentum loss rate due to Coulomb collisions [1].

In the case of low field side (LFS) launch, rays that dip below the operational window mode convert into fast waves that propagate radially outward, transporting power to the SOL and reducing η_{CD}. However, using the ray-tracing/Fokker–Planck codes GENRAY [13]/CQL3D [14], it has been found that due to a HFS launch effect, these fast waves can be made to mode convert back to slow waves prior to reaching the SOL. This allows mode conversion to be a beneficial process in the DIII-D HFS LHCD experiment that provides the upshift necessary for single-pass damping. The reduction of N_{acc} at the HFS is still required as mode conversion too close to the edge will be shown to be deleterious.

2. Mode conversion as a mechanism for upshift

Because the slow and fast waves propagate in opposite directions radially, the radial wave vector $k_r \to 0$ as the waves approach mode conversion. As this occurs, the wave does not propagate far and thus sees approximately constant plasma conditions. Thus, even with the changes in $N_\parallel$, the perpendicular wave vector $k_\perp$ does not vary substantially. The poloidal wave vector $k_\theta \propto m$ must therefore increase to balance the decrease in k_r. The resulting larger m is beneficial in two ways: it directly increases $N_\parallel$ (see equation (1)), and speeds further upshift due to $\mathrm{d}N_\parallel/\mathrm{d}t \propto \mathrm{d}m/\mathrm{d}t \propto m$, where under the assumption of a circular plasma and in the electrostatic limit, dm/dt is found from [9] to be

$$\frac{\mathrm{d}m}{\mathrm{d}t} \approx \frac{\omega r \sin(\theta)}{R}\left(\frac{\omega_{\mathrm{pe}}^2}{\Omega_{\mathrm{e}}^2 + \omega_{\mathrm{pe}}^2} + \frac{1}{k_\parallel}\left(\frac{m}{R_0 q} - \frac{n}{R}\right)\right). \tag{3}$$

Here, r is the minor radius and θ is the poloidal angle.

These effects are illustrated in figure 2, which shows the evolution of $N_\parallel$ (black), the poloidal contribution to $N_\parallel$ (cyan), the toroidal contribution (orange), and the accessibility condition (green) for a ray from figure 5(b). $N_\parallel$ follows N_ϕ closely up until $N_\parallel = N_{\mathrm{acc}}$ when $|N_\theta| \propto |m|$ grows considerably due to mode conversion. The following evolution of $N_\parallel$ is then largely driven by the evolution of N_θ. In this case, $|N_\theta|$ grows quickly enough to produce sufficient upshift for

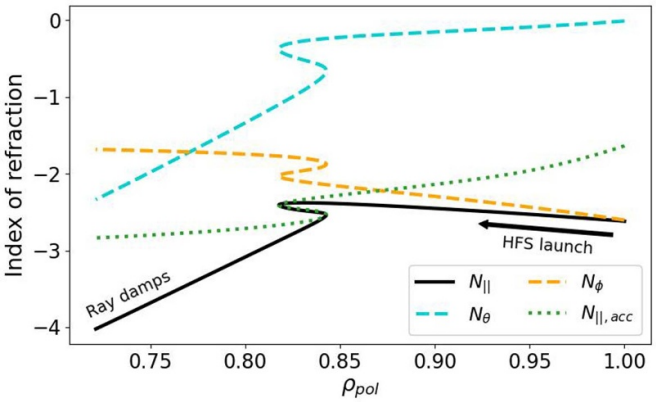

Figure 2. Example evolution of $N_{||}$, N_ϕ, and N_θ for a simulated ray in DIII-D discharge 147634 with $N_{||,\text{launch}} = -2.7$.

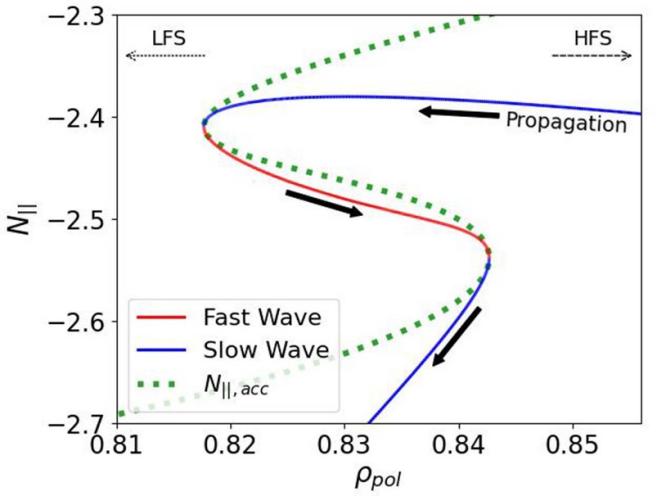

Figure 3. Zoomed in view of the mode conversion region in figure 2. The thick arrows show the propagation direction.

single-pass damping. An important feature seen more clearly in figure 3 is that there are two intersections of $|N_{||}|$ and N_{acc} and thus two mode conversions: slow $\rightarrow$ fast and then fast $\rightarrow$ slow. If mode conversion is positioned correctly (discussed in the following section), the waves remain fast for only a short period of time and do not propagate back to the SOL.

While the increase in $|m|$ due to mode conversion occurs for either LFS or HFS launch, the second mode conversion is only possible for HFS launch. When launching from the HFS, B decreases along the ray trajectory, causing $N_{\text{acc}} \propto 1/B$ to increase. After mode converting to the fast wave, the $|N_{||}|$ upshift is not fast enough to outpace the growth of N_{acc}, leading to the second mode conversion (see figure 3). In the case of LFS launch, N_{acc} decreases along the ray trajectory, preventing any second intersection between $|N_{||}|$ and N_{acc}.

A concern of relying on mode conversion to achieve the necessary upshift is the possibility of conversion efficiencies below unity. While such an effect is not captured in the ray-tracing simulations shown in the following section, [15] contains a comparison between a full-wave and ray-tracing simulation of HFS LHCD in DIII-D discharge 174658, which exhibits this double mode conversion phenomenon. Agreement between these simulations was found to be excellent, so substantial power loss during mode conversion is not expected. This also demonstrated that the presence of the $k_r \rightarrow 0$ caustic, where the ray-tracing approximation breaks down, does not negatively impact the accuracy of the ray-tracing simulations.

Table 1. On-axis values of the electron temperature, electron density, and magnetic field for the parameter scans discharges.

Discharge	T_{e0} (keV)	n_{e0} (m^{-3})	B_0 (T)
190316	6.16	$1.2 \cdot 10^{19}$	1.87
147634	4.5	$6.16 \cdot 10^{19}$	1.57
182659	3.42	$6.45 \cdot 10^{19}$	2.01

3. Optimization of ray trajectories

In addition to increasing $|m|$, mode conversion also affects dm/dt through the $\sin(\theta)$ term. By changing the location at which mode conversion occurs, the resulting ray trajectories may vary significantly. This location can therefore be optimized to produce rays that dwell in regions of high $|\sin(\theta)|$, resulting in increased upshift. From equation (2*a*), there are three main parameters that determine where mode conversion occurs: n_e, $N_{||,\text{launch}}$, and B. The result of scanning these parameters in GENRAY/CQL3D simulations of discharges 190316, 147634, and 182659 are shown in figures 4–6, respectively. 190316 is an ECH-only L-mode plasma; 147634 is a low $q_{\min}$ plasma and was the target plasma for optimization of the HFS LHCD launcher's design; and 182659 is a wide-pedestal QH-mode plasma. The on-axis temperature, density, and magnetic field of the discharges in these scans are given in table 1.

In figure 4 are ray trajectories for DIII-D discharge 190316, where the density is multiplied by a factor of 1, 1.5, and 2 times the experimental value and $N_{||,\text{launch}} = 2.3$. The temperature profiles and magnetic equilibrium are held constant over this scan. Higher densities result in mode conversion farther radially outward due to the increased N_{acc}. As this occurs, the poloidal projections of the ray trajectories become less flat and thus spend more time in the region where $\sin(\theta) \approx 1$, increasing the upshift and amount of single-pass damping. Additionally, upshift is further increased at higher density in this shot due to its low starting density. The $\omega_{pe}^2/(\Omega_e^2 + \omega_{pe}^2)$ term in equation (3) has not yet limited towards 1 and thus grows as density increases. At high enough densities, the rays mode convert too close to the edge and some do not single-pass damp.

While the increased rate of Coulomb collisions reduces the efficiency of LHCD at higher density ($\eta_{\text{CD}} \propto 1/n_e$), increasing densities may result in improved efficiency by improving the single-pass absorption. Because power loss in the SOL is

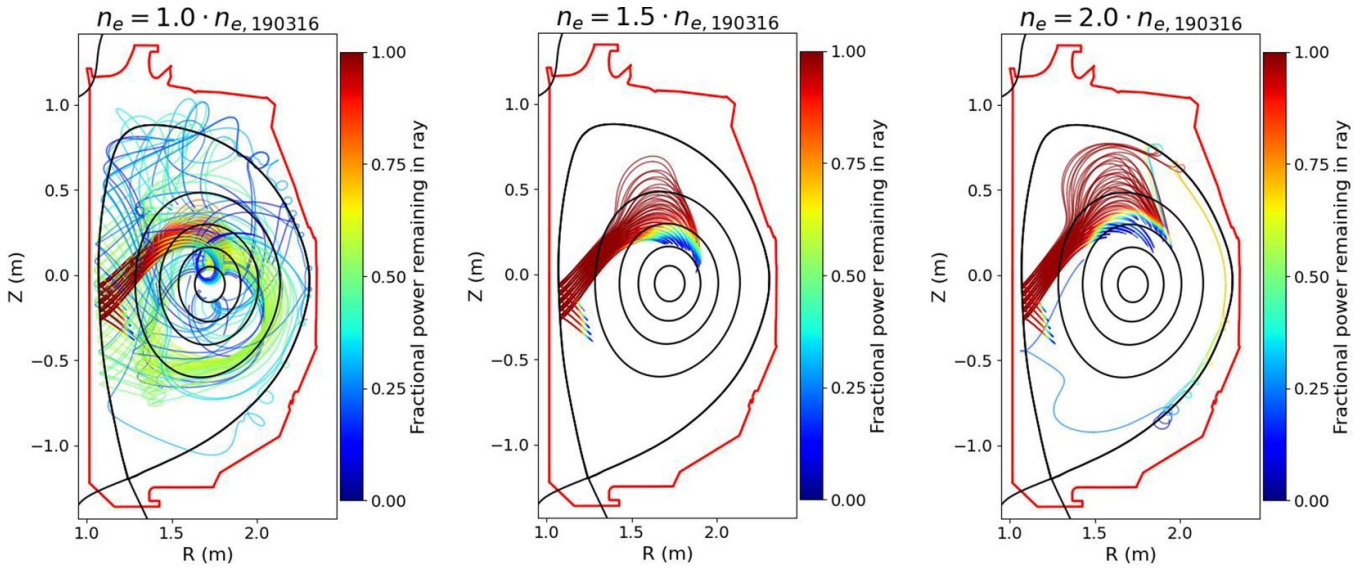

Figure 4. GENRAY/CQL3D ray trajectories for a density scan of DIII-D discharge 190316 with $N_{\|,\mathrm{launch}} = -2.3$. The equilibrium and temperature profiles are kept fixed.

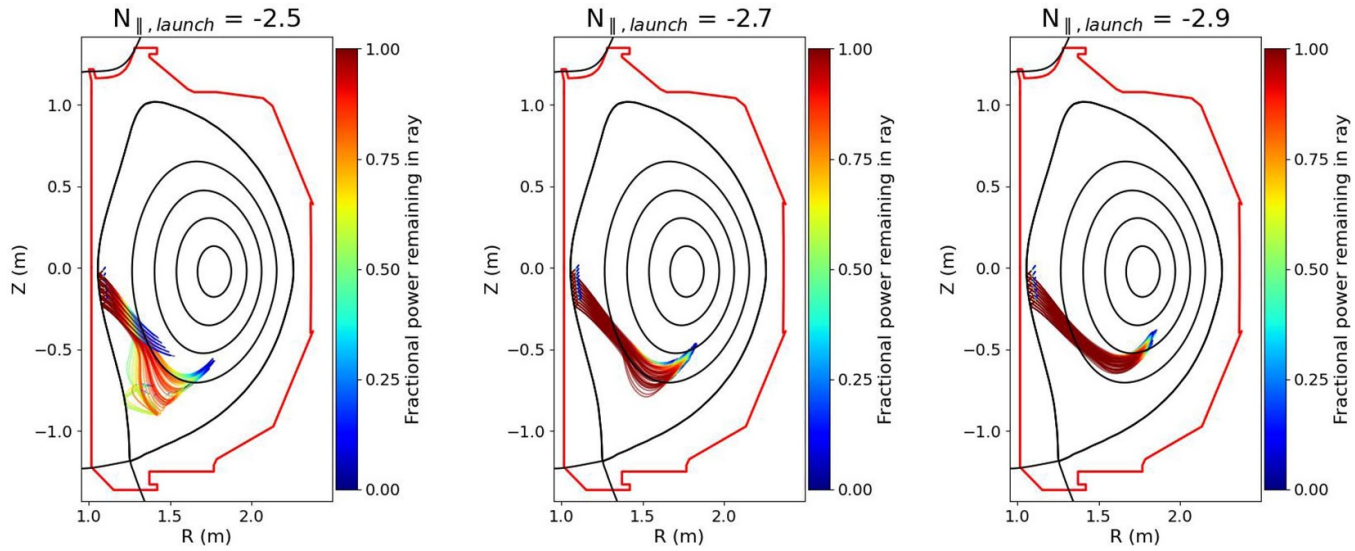

Figure 5. GENRAY/CQL3D ray trajectories for a $N_{\|,\mathrm{launch}}$ scan for DIII-D discharge 147634.

known to occur for LHCD, a larger fraction of power damped in the first pass, f_{SPA}, will result in more current being driven. A metric that incorporates both these effects is thus $f_{\mathrm{SPA}} \cdot \eta_{\mathrm{CD}} \propto f_{\mathrm{SPA}}/n_{\mathrm{e}}$. Figure 7 shows the dependence of this metric on density for 190316 with $N_{\|,\mathrm{launch}} = 2.3$, where f_{SPA} only considers power in the forward lobe. Below $\bar{n}_{\mathrm{e}}/\bar{n}_{\mathrm{e},190316} \approx 1.4$, the growth of f_{SPA} due to the improved upshift outpaces $1/n_{\mathrm{e}}$. Increasing the density in this regime would likely increase the driven current. Beyond this point, f_{SPA} reaches 1 and then begins to decrease due to worsening ray trajectories, resulting in a falloff of $f_{\mathrm{SPA}}/n_{\mathrm{e}}$ faster than $1/n_{\mathrm{e}}$. The exact behavior of $f_{\mathrm{SPA}}/n_{\mathrm{e}}$ is dependent on the discharge. Note this scan was completed assuming no decrease in T_{e} as n_{e} was raised. If this is not possible in experiment due to insufficient heating power, the region in which density may be beneficial to current drive is likely to end at a lower density.

The ray trajectories for DIII-D discharge 147634 for $N_{\|,\mathrm{launch}} = -2.5$, -2.7, and -2.9 are shown in figure 5. The change in sign of $N_{\|}$ relative to 190316 is due to reversal of the toroidal magnetic field direction. Reducing $|N_{\|,\mathrm{launch}}|$ moves mode conversion radially outward since $N_{\|}$ is initially closer to N_{acc}. If mode conversion occurs too far radially outward, as in figure 5(a), some rays hit the LCFS as they bounce outward, decreasing the single-pass absorption. Comparing the deposition locations in these three cases, a larger $|N_{\|,\mathrm{launch}}|$ damps nearer to the core. This is opposite of the expected behavior, where a larger $|N_{\|,\mathrm{launch}}|$ requires colder electrons to damp and thus should damp closer to the edge. But smaller $|N_{\|,\mathrm{launch}}|$

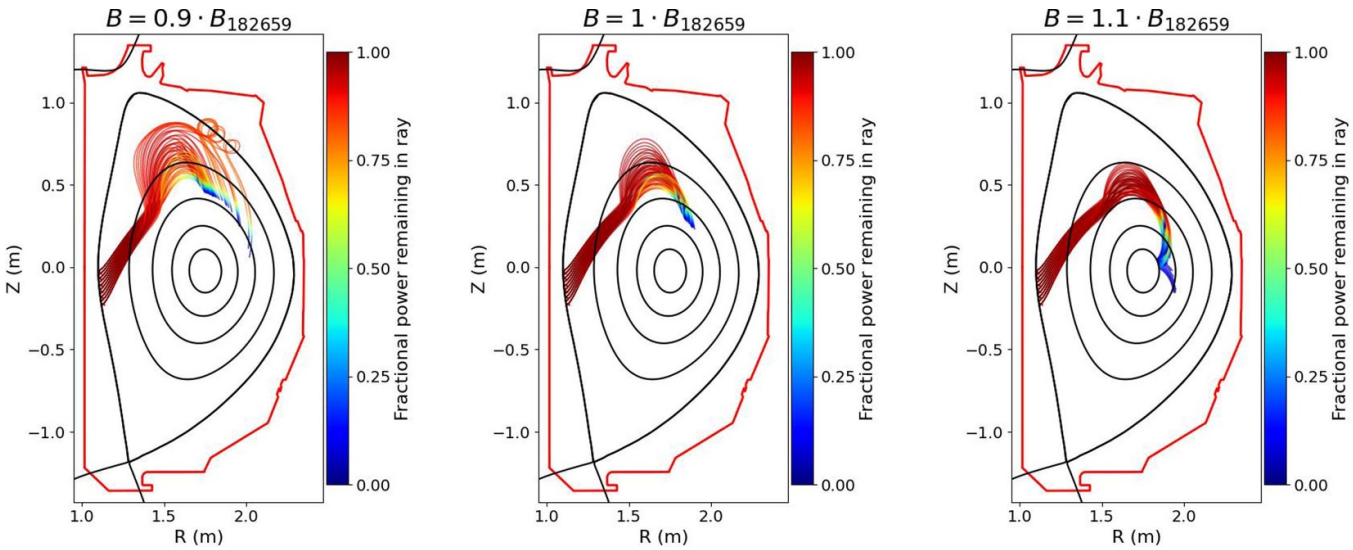

Figure 6. GENRAY/CQL3D ray trajectories for a magnetic field strength scan for DIII-D discharge 182659 and $N_{\|,\text{launch}} = 2.9$. The toroidal and poloidal fields are scaled equally to keep the safety factor unchanged.

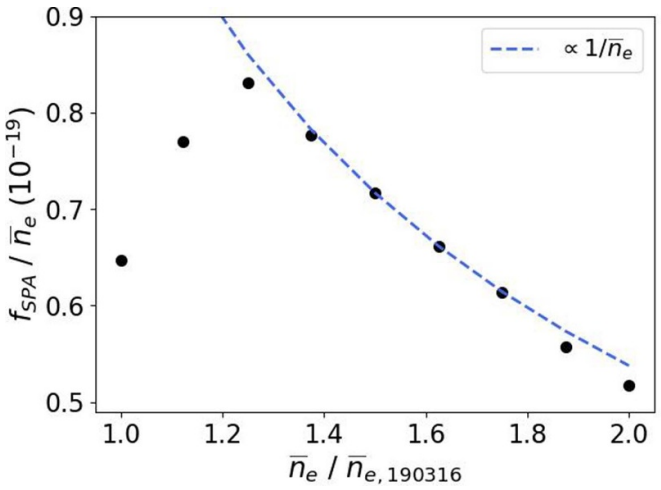

Figure 7. Dependence on density of the ratio of the fraction of power damped in the first pass by the forward lobe to the line averaged density for DIII-D discharge 190316 and $N_{\|,\text{launch}} = 2.3$.

mode convert earlier and experience sufficient upshift to damp soon after, depositing their power closer to the edge. The average $N_{\|}$ at which the waves damp in figures 5(a)–(c) are −4.3, −3.77, and −3.62, respectively. The final scan is given in figure 6, which shows DIII-D discharge 182659 with its magnetic field scaled by a factor of 1, 1.1, and 1.2 for $N_{\|,\text{launch}} = 2.9$. Increasing the magnetic field moves mode conversion radially inward due to the reduced N_{acc}.

4. Future experimental confirmation

During the 2023 vent, a new hard x-ray (HXR) camera was installed as a dedicated diagnostic for the HFS LHCD system. The camera consists of 32 tangential viewing Kromek SPEAR™ Cadmium Zinc Telluride (CZT) detectors capable of measuring bremsstrahlung radiation emitted by LHCD-generated fast electrons in the HXR range (50–250 keV). By inverting the line-integrated measurements in one dimension, the HXR emissivity profile is recovered, which acts as a proxy for the power deposition profile. More details of the camera are provided in [16].

Some aspects of the camera have been updated since publication of [16]. The Gaussian shaping amplifiers are now a modified version of those detailed in [17], where the gain has been reduced from 1008 to 710, and the ∼1 μs wide pulses have been shortened to ∼800 ns. Additionally, improved etendue calculations have led to lower expected count rates. At full power and for the single-pass cases detailed in the previous section, the median time resolution of the 32 sightlines required for less than 10% statistical error ranges from 0.1–20 ms. This camera will verify that GENRAY/CQL3D correctly predict the propagation and absorption of the LH waves through comparing the measured HXR emissivity profile against that predicted by CQL3D's synthetic x-ray diagnostic for a set of scans over $N_{\|,\text{launch}}$, n_e, and/or B.

Targets for these scans will be selected such that each plasma has a distinctly different emissivity profile (as predicted by GENRAY/CQL3D), allowing the evolution of the inversion to be seen throughout the scan. Of note is that the discharges chosen for the scans in section 3 were selected for demonstration of single-pass absorption in a variety of plasmas and are not necessarily the optimal plasmas in which to verify this double mode conversion effect.

Comparisons between simulated and experimental HXR emissivity profiles have been completed for previous LFS LHCD experiments, and generally poor agreement was found [18–20]. This is typically attributed to repeated SOL interactions resulting from operation in the multi-pass regime [20, 21]. The scans to be completed on DIII-D will contain

both points in the single-pass and multi-pass regime. If SOL interactions are to blame, the single-pass points should exhibit greater accuracy of simulation. If good agreement is reliably obtained in these single-pass discharges, GENRAY/CQL3D would be shown to properly model the LHCD physics. This would bode well for the use of GENRAY/CQL3D to predict HFS LHCD in a reactor, especially because a reactor-grade plasma will not require this mode conversion effect (therefore being simpler to model), and full-wave phenomena are unlikely to be important [15, 22].

5. Conclusion

Single-pass damping in the DIII-D HFS LHCD experiment is achieved through the LH waves mode converting twice, made possible only by launching from the HFS. Through varying $N_{\|,\mathrm{launch}}$, n_e, and/or B, the location of mode conversion can be optimized such that ray trajectories result in sufficient upshift for single-pass damping. Counter-intuitively, increasing density may result in greater current driven in some cases, and smaller $|N_\||$ tend to damp closer to the edge. A new HXR camera will validate these predictions during the DIII-D 2024 campaign through comparison of HXR emissivity profiles to simulation.

Data availability statement

All data that support the findings of this study are included within the article (and any supplementary files).

Acknowledgment

This work is supported by the U.S. Department of Energy, Office of Science, Office of Fusion Energy Sciences, using User Facility DIII-D, under Award Number DE-FC02-04ER54698, US DoE Award SC0014264, and by US DoE Contract No. DE-FC02-01ER54648 under a Scientific Discovery through Advanced Computing Initiative. Disclaimer: This report was prepared as an account of work sponsored by an agency of the United States Government. Neither the United States Government nor any agency thereof, nor any of their employees, makes any warranty, express or implied, or assumes any legal liability or responsibility for the accuracy, completeness, or usefulness of any information, apparatus, product, or process disclosed, or represents that its use would not infringe privately owned rights. Reference herein to any specific commercial product, process, or service by trade name, trademark, manufacturer, or otherwise does not necessarily constitute or imply its endorsement, recommendation, or favoring by the United States Government or any agency thereof. The views and opinions of authors expressed herein do not necessarily state or reflect those of the United States Government or any agency thereof.

ORCID iDs

Grant Rutherford https://orcid.org/0000-0001-6362-0037
Samuel J Frank https://orcid.org/0000-0001-8414-6987
Andrew H Seltzman https://orcid.org/0000-0002-7725-2981

References

[1] Fisch N J 1987 *Rev. Mod. Phys.* **59** 175
[2] Bécoulet A *et al* 2011 *Fusion Eng. Des.* **86** 490
[3] Wallace G *et al* 2011 *Nucl. Fusion* **51** 083032
[4] Faust I C *et al* 2016 *Phys. Plasmas* **23** 056115
[5] Ding B *et al* 2018 *Nucl. Fusion* **58** 095003
[6] Seltzman A, Shiraiwa S, Wallace G and Wukitch S 2019 *Nucl. Fusion* **59** 096003
[7] Wukitch S J, Shiraiwa S, Wallace G M, Bonoli P T, Holcomb C and Pinsker R I 2017 *EPJ Web Conf.* **157** 02012
[8] Seltzman A and Wukitch S 2020 *Fusion Eng. Des.* **159** 111762
[9] Bonoli P 1984 *IEEE Trans. Plasma Sci.* **12** 95
[10] Golant V E 1972 *Sov. Phys.-Tech. Phys.* **16** 1980–8 (Engl. transl.)
[11] Porkolab M 1984 *IEEE Trans. Plasma Sci.* **12** 107
[12] Bonoli P *et al* 2018 *Nucl. Fusion* **58** 126032
[13] Smirnov A and Harvey R 1995 *Bull. Am. Phys. Soc.* **40** 35
[14] Harvey R and McCoy M 1992 *Proc. IAEA Technical Committee Meeting on Simulation and Modeling of Thermonuclear Plasmas* pp 489–526
[15] Frank S J, Wright J C, Hutchinson I H and Bonoli P T 2022 *Plasma Phys. Control. Fusion* **64** 105023
[16] Rutherford G, Seltzman A H and Wukitch S J 2022 *Rev. Sci. Instrum.* **93** 103529
[17] Liptac J E 2006 Lower hybrid modeling and experiments on alcator C-mod *PhD Thesis* Massachusetts Institute of Technology
[18] Schmidt A, Bonoli P T, Meneghini O, Parker R R, Porkolab M, Shiraiwa S, Wallace G, Wright J C, Harvey R W and Wilson J R 2011 *Phys. Plasmas* **18** 056122
[19] Peysson Y *et al* 2016 *Plasma Phys. Control. Fusion* **58** 044008
[20] Biswas B, Baek S G, Bonoli P, Shiraiwa S, Wallace G and White A 2020 *Plasma Phys. Control. Fusion* **62** 115006
[21] Baek S G 2014 Detection of lower hybrid waves at the plasma edge of a diverted tokamak *PhD Thesis* Massachusetts Institute of Technology
[22] Frank S, Lee J, Wright J, Hutchinson I and Bonoli P 2022 *J. Plasma Phys.* **88** 905880603